ADVANCED FUNCTIONAL MATERIALS
www.afm-journal.de

High-Performance Magnetic FePt ($L1_0$) Surface Microrollers Towards Medical Imaging-Guided Endovascular Delivery Applications

*Ugur Bozuyuk, Eylul Suadiye, Amirreza Aghakhani, Nihal Olcay Dogan, Jelena Lazovic, Mehmet Efe Tiryaki, Martina Schneider, Alp Can Karacakol, Sinan Ozgun Demir, Gunther Richter, and Metin Sitti**

Controlled microrobotic navigation in the vascular system can revolutionize minimally invasive medical applications, such as targeted drug and gene delivery. Magnetically controlled surface microrollers have emerged as a promising microrobotic platform for controlled navigation in the circulatory system. Locomotion of microrororollers in strong flow velocities is a highly challenging task, which requires magnetic materials having strong magnetic actuation properties while being biocompatible. The $L1_0$-FePt magnetic coating can achieve such requirements. Therefore, such coating has been integrated into 8 µm-diameter surface microrollers and investigated the medical potential of the system from magnetic locomotion performance, biocompatibility, and medical imaging perspectives. The FePt coating significantly advanced the magnetic performance and biocompatibility of the microrollers compared to a previously used magnetic material, nickel. The FePt coating also allowed multimodal imaging of microrollers in magnetic resonance and photoacoustic imaging in ex vivo settings without additional contrast agents. Finally, FePt-coated microrollers showed upstream locomotion ability against 4.5 cm s^{-1} average flow velocity with real-time photoacoustic imaging, demonstrating the navigation control potential of microrollers in the circulatory system for future in vivo applications. Overall, $L1_0$-FePt is conceived as the key material for image-guided propulsion in the vascular system to perform future targeted medical interventions.

1. Introduction

Wireless microrobots possess significant potential to revolutionize minimally invasive targeted medical applications in hard-to-reach, unprecedented and risky regions inside the human body.[1] The circulatory system is an obvious route for medical microrobots to reach any tissue or organ in the body; however, strong fluid flows are the most significant barrier to controlled navigation inside the blood vessels.[2] Surface rolling magnetic microrobots or surface microrollers have emerged as a promising microrobotic platform for controlled navigation in the circulatory system, which takes advantage of decreased flow velocities at the vessel walls.[3,4] So far, the locomotion ability of the cell-sized microrobots is limited to the vessels with relatively low flow velocities, such as post-capillary venules.[3,5] The magnetic material used in the microrollers is one of the main limiting factors for locomotion against stronger fluid flows.[3] The commercially available coating materials, such as Ni and Co, possess low remanence that is unfavorable for actuation with weak uniform fields. The materials used in the microrollers must also be biocompatible, while the biocompatibility of Ni- and Co-based magnetic materials is highly debatable.[6,7] $L1_0$ phase of FePt is a promising hard-magnetic material for micro/nanosystems, which offers high remanence, coercivity, biocompatibility, and stability.[8] It was

U. Bozuyuk, A. Aghakhani, N. O. Dogan, J. Lazovic, M. E. Tiryaki, M. Schneider, A. C. Karacakol, S. O. Demir, M. Sitti
Physical Intelligence Department
Max Planck Institute for Intelligent Systems
70569 Stuttgart, Germany
E-mail: sitti@is.mpg.de

The ORCID identification number(s) for the author(s) of this article can be found under https://doi.org/10.1002/adfm.202109741.

DOI: 10.1002/adfm.202109741

U. Bozuyuk, N. O. Dogan, M. E. Tiryaki, M. Sitti
Institute for Biomedical Engineering
ETH Zurich
Zurich 8092, Switzerland

E. Suadiye, G. Richter
Materials Central Scientific Facility
Max Planck Institute for Intelligent Systems
70569 Stuttgart, Germany

M. Sitti
Koç University
School of Medicine & College of Engineering
Istanbul 34450, Turkey

implemented in different nanofabrication schemes,[9] thus; it could be integrated into the microrollers to benefit from their distinct advantages. Owing to its unique properties such as high remanence and biocompatibility, it seems to be a suitable match to the surface microrollers for endovascular applications: High remanence would allow navigation at higher flow velocities due to better actuation in weak rotating magnetic fields, and biocompatibility will ensure the safer utilization of the microrollers inside the human body.

Precise localization of the microrobots in the body is only possible with suitable medical imaging feedback for robot tracking and control.[10] Although considerable progress has been made, real-time in vivo imaging of single or a swarm of cell-scale microrobots is a grand challenge.[11] Several medical imaging modalities are available for microrobots; however, there is no single "ideal" imaging modality. Each technique has distinct advantages and disadvantages, and selecting the appropriate imaging modality depends on several factors.[10] Multimodal imaging contrast materials possess a critical role in biomedical research since they make it possible to take advantage of different imaging techniques. FePt-based materials have been previously used as contrast agents for different imaging modalities, such as magnetic resonance imaging (MRI),[12] photoacoustic imaging (PA),[13] and X-ray microtomography[14] due to their high-contrast magnetic and optical properties.[14] Thus, FePt-coated microrobots could also offer multimodal imaging capability, which has not been explored previously to the best of our knowledge. Surface microrollers must be traceable in realistic in vivo conditions with different imaging modalities for specific medical applications.

Here, we report the integration of ferromagnetic FePt ($L1_0$) alloy nanofilms to surface microrollers. Magnetically actuated Janus surface microrollers are composed of 8 µm diameter silica particles, half-coated with FePt alloy with three different film thicknesses (60, 120, and 480 nm), which were coated in a molecular beam epitaxy system (**Figure 1**). The alloy was formed after co-deposition of Fe and Pt followed by an annealing step (Figure 1A). The FePt-coated microrollers outperformed the previous magnetic film material (Ni) used, resulting in higher remanence and coercivity. The FePt-coated microrollers have also shown strong biocompatibility with macrophages and endothelial cells. The cross-platform medical imaging potential of the FePt-coated microrollers was also investigated in MRI and PA imaging modalities in ex vivo settings. A very low number of microrollers were even detectable thanks to FePt-coating, without employing additional contrast agents. To demonstrate the high locomotion performance of the FePt-coated microrollers, as a proof-of-concept, we performed upstream locomotion experiments at 4.5 cm s^{-1} average flow velocity along with real-time PA imaging. The results demonstrated the multifunctionality and suitability of the FePt coatings towards next-generation surface microrollers to be used in future medical applications, such as targeted drug/gene delivery,[3] aneurysm treatment,[15] and fibrinolytic therapy.[16]

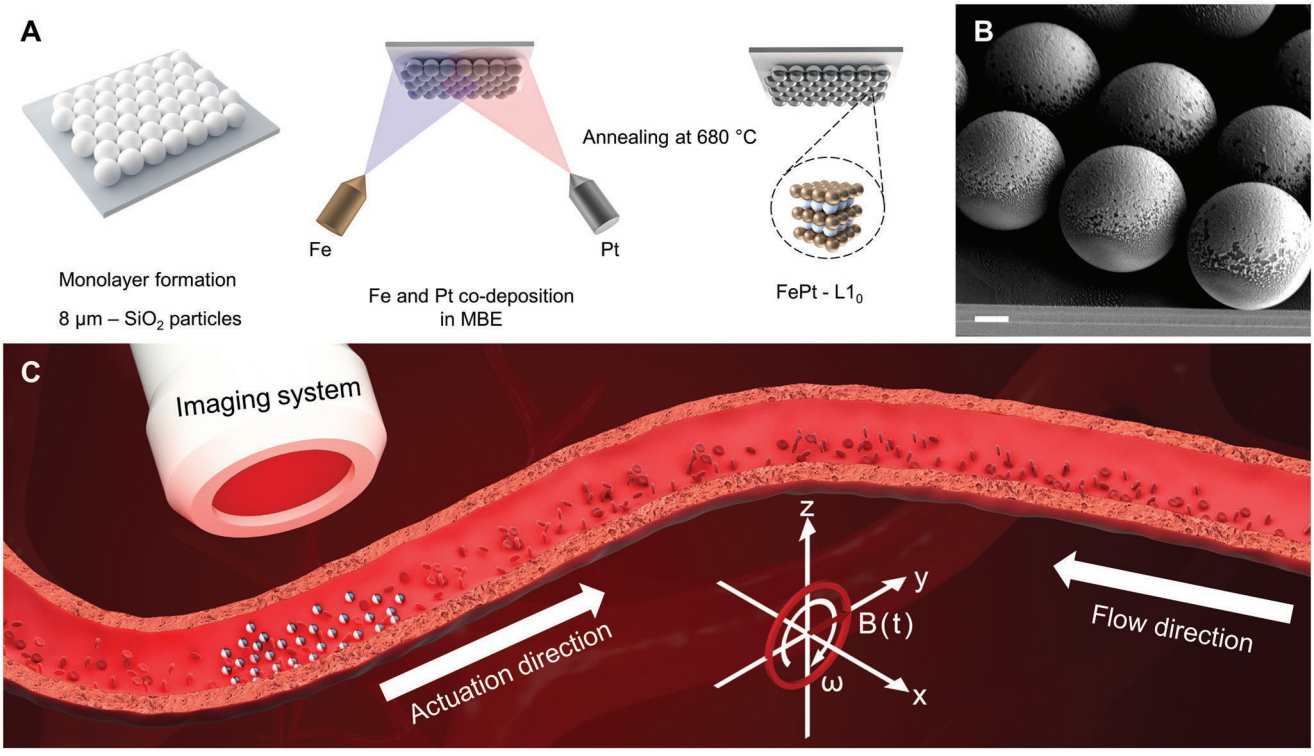

Figure 1. FePt ($L1_0$)-coated microrollers towards endovascular navigation applications. A) Schematic representation of the molecular beam epitaxy (MBE) process to fabricate high-performance microrollers. Self-assembled 8 µm-diameter SiO_2 particle monolayer on a Si substrate followed by an MBE co-deposition of Fe and Pt. The FePt-$L1_0$ was formed with a single annealing step at 680 °C. B) Scanning electron microscopy (SEM) image of the 60 nm-thick FePt-coated microrollers. Scale bar: 2 µm. C) Conceptual schematic illustration of the magnetic microrollers navigating in the vascular system, along with an integrated medical imaging modality.

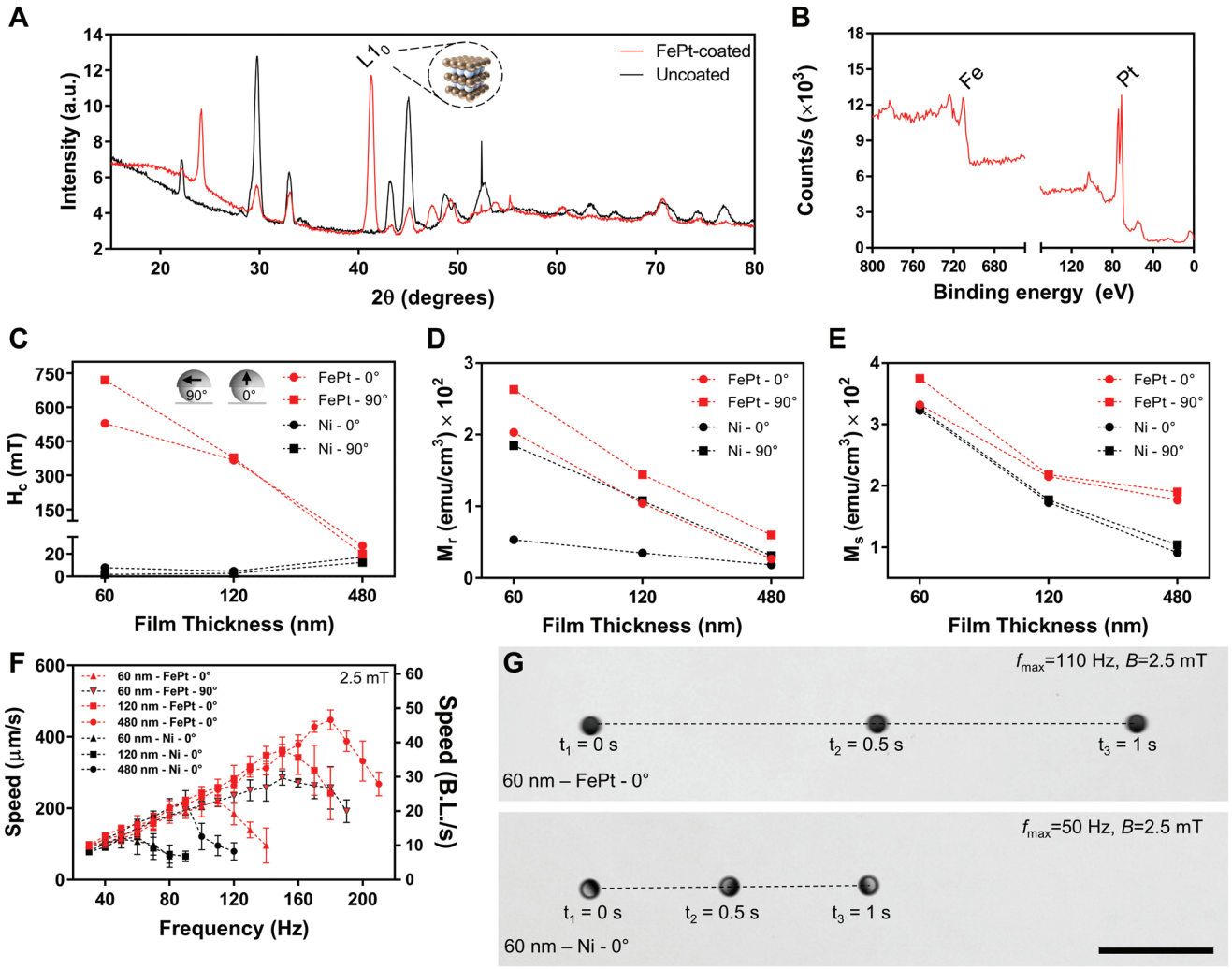

Figure 2. Structural (XRD), chemical (XPS), and magnetic (VSM) characterization of the FePt-coated microrollers. A) Structural characterization of the thin film after the deposition process, characterized with XRD. $L1_0$ peak was identified at 42° after the deposition and annealing. B) XPS survey scan of the thin film. The atomic ratio of Fe and Pt was 47%, 53%, respectively. C–E) VSM characterization results of FePt-$L1_0$ and Ni coating at different thicknesses (60, 120, and 480 nm). The inset shows the in-plane (90°) and out-of-plane (0°) directions. The overall efficiency of the thin film decreased with the increasing thickness (H_c = coercivity, M_r = remanence, M_s = saturation magnetization at 1.8 T). F) Average translational speeds of the microrollers with different film thicknesses. The FePt-coated microrollers outperformed their Ni-coated counterparts. 480 nm-thick FePt-coated group could reach up to 180 Hz at 2.5 mT, corresponding to around 50 body lengths per second (BLS). The error bars represent the standard deviation of the mean. G) The time-lapse images of the 60 nm-thick FePt- and Ni-coated microrollers at their maximum rotation frequency at 2.5 mT. The FePt-coated microroller was at least two times faster than the Ni-coated one. Scale bar: 50 μm.

2. Results and Discussions

2.1. Film Characterization

FePt-coated microrollers were fabricated using a molecular beam epitaxy system. Fe and Pt were deposited on the monolayered silica particles, followed by an in situ heat treatment step at 680 °C for the $L1_0$ phase formation. The structural evolution of $L1_0$ was characterized with X-ray diffraction (XRD) analysis. The $L1_0$ peak was identified from theta-2theta scans and locked couple measurements for the three different film thicknesses at 42° (**Figure 2**A, Figure S1, Supporting Information). Next, the chemical composition of the FePt-$L1_0$ films was characterized using X-ray photoelectron spectroscopy (XPS) (Figure 2B). The survey scan measurements revealed that the thin film had a 47% to 53% (±2%) ratio of Fe and Pt, respectively. According to the Fe–Pt phase diagram, the ratio satisfies the requirements to obtain $L1_0$ phase.[17] In addition, an energy-dispersive X-ray spectroscopy mapping has shown a homogenous distribution of the Fe and Pt on the thin film (Figure S2, Supporting Information).

After structural and chemical characterization, the magnetic properties of the FePt-coated microrollers with three different thicknesses were characterized using a vibrating sample magnetometer (VSM) (Figure 2C–E). The magnetic properties of the previously used magnetic material Ni, were also characterized for comparison. The measurements were performed in two orientations: in-plane (90°) and out-of-plane (0°) configurations. 60 nm-thick FePt film resulted in the highest coercivity

in both configurations, while the coercivity of the Ni was much lower in all thicknesses as expected (Figure 2C). The in-plane (90°) configuration naturally resulted in higher coercivity than the out-of-plane (0°) FePt film. The coercivity of the FePt film had a decreasing trend with increasing thickness. This trend can be explained by the thickness and the magnetic domain structure of the thin films.

Scanning electron microscope (SEM) image analysis of the microrollers with three different thicknesses demonstrated a gradual growth of the film on the silica microspheres (Figure 1B, Figure S3, Supporting Information). 60 nm-thick FePt-$L1_0$ film resulted in partial coverage as a nanoparticle-like film (Figure 1B), where the film was continuous and homogeneous for the 120 nm-thick case (Figure S3A,B, Supporting Information). On the other hand, the film was a rough and layered inhomogeneous film for the 480 nm-thick case (Figure S3C,D, Supporting Information). Therefore, we can discuss the observed coercivity behavior in the context of particle diameter-coercivity relation, which was discussed and explained in the literature before.[18] Namely, the critical single/multi-domain diameter zone on the silica was passed with increasing film thickness as the grains of the FePt film was growing. For example, the multi/single-domain transition of $L1_0$-$Fe_{50}Pt_{50}$ nanoparticles was around 180 nm.[19] Beyond this size, a full three-dimensional (3D) magnetic domain structure is formed, reducing the magnetic field around the particles. It should also be noted that the heat treatment to obtain the $L1_0$ phase impacts grain growth. The remanence of the thin films followed a similar trend; the efficiency decreased with increasing film thicknesses, whereas the FePt film had higher remanence than Ni film for both configurations (Figure 2D). Again, in-plane configuration (90°) resulted in higher remanence for both FePt and Ni films in any thicknesses. The FePt film again had higher saturation magnetization at 1.8 T, yet, the hysteresis loop analysis has shown that the FePt films did not even reach the saturation at 1.8 T, which is the maximum field applied in our VSM system (Figure S4, Supporting Information). On the other hand, Ni has quickly reached saturation for both configurations (Figure S4, Supporting Information).

We characterized the locomotion behavior and performance of the Ni- and FePt-coated microrollers. The microrollers were actuated with weak rotating magnetic fields, specifically a 2.5 mT rotating field. The microrollers were magnetized to the out-of-plane (0°) direction under a 1.8 T uniform magnetic field, and they retained their magnetization at a 2.5 mT rotating field (Figure 2C). The micorollers followed the rotating magnetic field; the rotation of a microroller with a nearby wall resulted in translation at the low Reynolds number regime.[20] The microroller translational velocity linearly increases with the rotation frequency of the applied field until a critical threshold, the step-out frequency. The FePt-coated microrollers resulted in higher step-out frequencies due to their higher total remanence, while Ni-coated groups stepped-out very early (Figure 2F,G). The step-out frequencies of the different thicknesses were not linearly proportional to the film thickness, as expected. For example, 480 nm coated FePt microrollers stepped-out at 180 Hz at 2.5 mT, while 60 nm coated FePt microrollers stepped-out at 110 Hz. Although the film thickness increased eight-fold, the step-out frequency did not even increase two-fold. This is due to the decreased remanence of the thin film, which was explained previously.

In-plane (90°) magnetization of the microrollers resulted in higher efficiency from the VSM characterizations, which is also reflected in the step-out frequency results (Figure 2F, 60 nm–FePt–90°). However, in-plane magnetization resulted in slower microroller speeds at high frequencies than its counterparts (e.g., 480 nm–FePt–0°). This was probably due to misalignment of the rotation axis and center of mass at in-plane magnetization direction, which caused partially hindered microroller motion. The other crucial practical consideration is the magnetically induced aggregation of FePt-based microrollers. The microrollers with 480 nm-thick FePt coating had higher total remanence, and they resulted in big clusters at high concentrations of microrollers. At the same time, the aggregation was much less prominent for 60 nm-thick FePt-coated microrollers (Supporting Information Video S1). 60 nm-thick FePt-coated microroller aggregates were able to disaggregate upon actuation at high frequencies. The same did not happen to the 480 nm aggregates due to much stronger magnetic interaction. The aggregation problem of the microrollers could be solved by integrating a thick inert layer on top of the magnetic thin film to decrease the magnetic interactions between individual particles due to the increased effective distance in contacting particles. The 60 nm-coated FePt particles were used in the rest of the study.

2.2. Biocompatibility Tests

Material selection in microrobot design and fabrication is an essential consideration for using microrobots inside the human body since medical microrobots are designed to be used in the human body for short or long durations, continuously interacting with bodily tissues and cells. If any microrobotic system has poor biocompatibility with the bodily tissues, it will eventually cause various adverse effects, such as inflammation, carcinogenicity, and allergic response.[21] Therefore, the materials used in the microrobotic systems should not show any adverse and toxic effects to avoid severe short and long time consequences upon the microrobot deployment inside the body. The previous magnetic material, Ni, used in our microroller system was extensively studied in the literature[7] and is considered a toxic and allergenic material.[22] Therefore, we replaced it with FePt ($L1_0$) alloy in this study, where it also showed a higher magnetic performance.

Microparticle-based robots administrated into the blood vessels interact with endothelial cells and immune cells.[23] It has been widely shown that different silica-based microparticles caused negligible toxicity upon contact with endothelial cells.[24] On the other hand, macrophages, being the heart of the immune system, are much more sensitive and demonstrate various responses to different particle systems.[25] They readily uptake the foreign objects to maintain homeostasis in the body.[26] It was proposed that having an understanding between macrophages and particulates is crucial to predict the overall toxicity of the system in the body.[23] Therefore, we selected a macrophage cell line to assess the biocompatibility of the FePt-coated microrollers. We treated the macrophage (J774A.1) cell line with the uncoated Ni (60 nm Ni-20 nm Au)-coated and FePt (60 nm)-coated particle groups (**Figure 3**A).

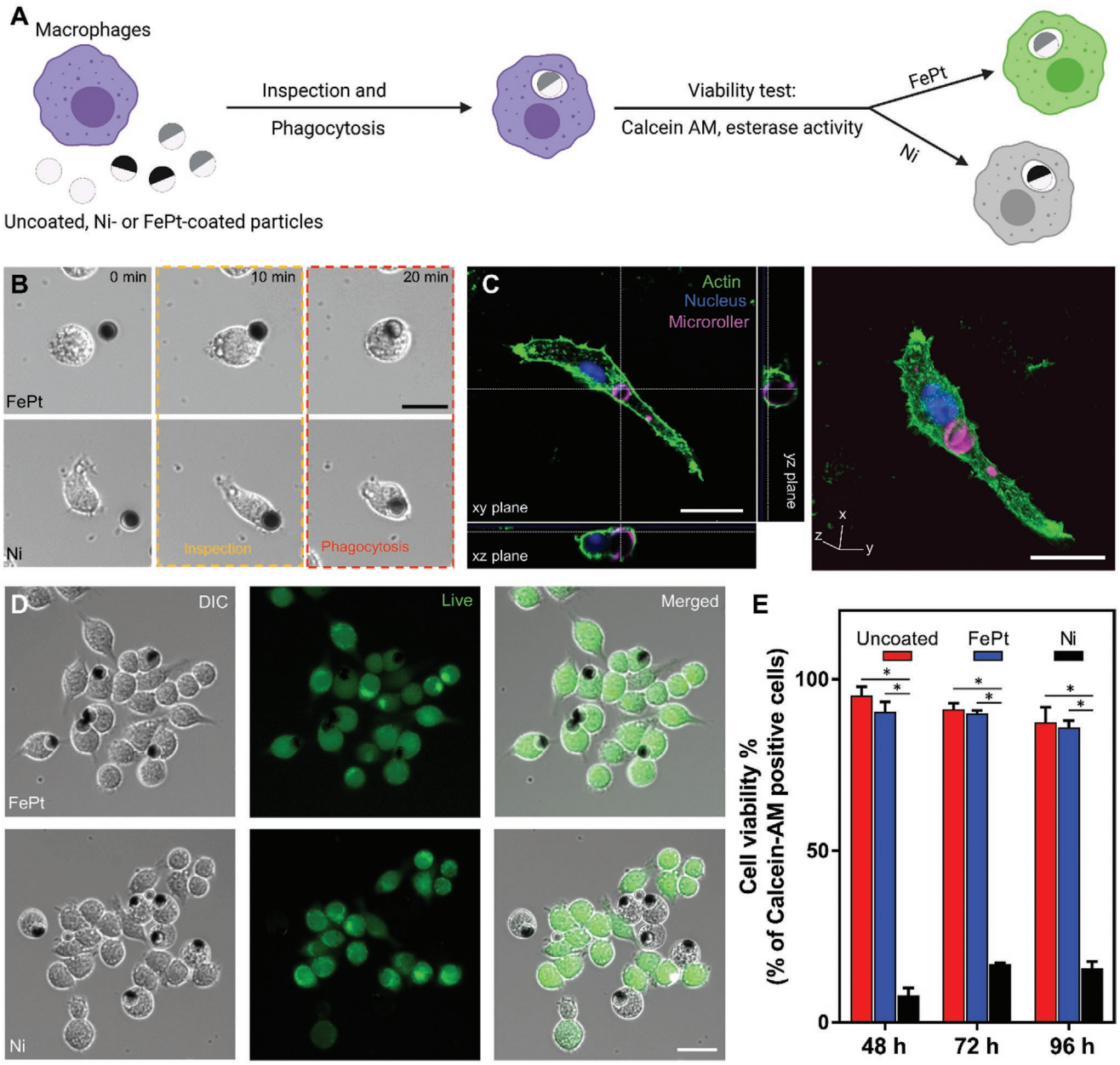

Figure 3. Biocompatibility test results with the macrophage (J774A.1) cell line. A) 60 nm-thick Ni- and FePt-coated microrollers were introduced to the macrophage cells with 1:10 particle to initial cell ratio. The macrophages engulfed the microrollers, ensuring the contact of the deposited thin film with the cells. After 48 h, the viability of the cells was evaluated based on the esterase activity of the cells. B) Time-lapse images of the phagocytosis of the different microroller groups. Both Ni and FePt microroller groups were quickly engulfed by the macrophages upon an inspection. Scale bar: 20 µm. C) Confocal microscopy images show engulfed FePt microroller by a macrophage. Scale bar: 20 µm. D) Microscopy images of the macrophages, 48 h after microroller addition. Ni engulfed macrophages did not show any viability while FePt-coated group was alive. Scale bar: 25 µm. E) The % viability of the cell-particle complexes that engulfed the particles were quantified based on their calcein-AM signal at different time points. The Ni group has shown poor viability, while the Si and FePt groups have shown more than 85% viability (*, Student's *t*-test, $p < 0.05$). The error bars represent the standard deviation of the mean.

Macrophage cell lines engulfed all the particles in a short duration, ensuring the continuous contact of the deposited material with the cells. The viability of the cells carrying a particle was assessed by live/dead (Calcein-AM/Ethidium homodimer-1) staining. After adding the particles to the macrophages, particles were engulfed by the macrophages upon a short inspection period (Figure 3B), and there was no free particle observed (Figure S5, Supporting Information). The confocal microscopy analysis also revealed a single FePt-coated microroller was fully engulfed by a single macrophage cell (Figure 3C). After 48, 72, and 96 h, macrophage cells with uncoated and FePt-coated microrollers have shown clear viability, same as the bare macrophages in the same culture environment (Figure 3D, Figures S6–S8, Supporting Information). On the other hand, macrophages with Ni-coated microrollers lost their viability, giving no Calcein-AM signal at 48, 72, and 96 h. Additionally,

the bare macrophages were alive in the same cultural environment (Figure 3D, Figures S6–S8, Supporting Information). However, they also did not give any ethidium homodimer-1 signal for all time points, indicating their cell membranes were not compromised enough for the given time points (Figures S6–S8, Supporting Information).

We analyzed the % cell viability, based on the calcein-AM positive cells, using the particle-engulfed macrophages. The analysis has revealed that the macrophages with uncoated or FePt-coated microrollers have shown more than 85% viability at 48, 72, and 96 h (Figure 3E). In comparison, the viability of the Ni-coated group had less than 20% at 48, 72, and 96 h (Figure 3E). Furthermore, we performed additional viability tests with macrophages and assessed the metabolic activity (ATP) of the whole population of macrophages depending on the number of FePt-coated microrollers. We added FePt-coated microrollers to macrophages in 10^3 microroller/10^4 initial cell and 5×10^3 microroller/10^4 initial cell number ratios, simulating low and high concentrations. After 72 h, both groups have shown more than 85% viability, demonstrating the further compatibility of the FePt-coated microrollers with macrophages (Figure S9, Supporting Information).

As described previously, endothelial cells are one of the major cell types in blood vessels, and biocompatibility of the microrollers must also be tested with endothelial cells. Therefore, we performed viability tests with human umbilical vein endothelial cells (HUVECs) in static and dynamic settings. In static settings, we added FePt-coated microrollers on top of the HUVECs in 10^3 microroller/10^4 initial cell and 5×10^3 microroller/10^4 initial cell number ratio. We tested the viability of the cells based on live/dead staining and metabolic activity. In both concentrations, HUVECs were alive (Figure S10A, Supporting Information) and have shown more than 90% viability after 72 h (Figure S10B, Supporting Information).

Locomotion of microrollers on endothelial cells may also cause adverse effects due to forces exerted on the cells by the microrollers. When a microroller moves, it exerts propulsion force to its translational direction and gravitational force on the bottom wall.[3,4] The order of these forces is at pN level on our size scale,[3] whereas rupture of the endothelial cell membrane needs hundreds of nN forces.[27] The other important consideration is that the microrollers interact momentarily with endothelial cells in an in vivo scenario since their translational speeds are very high. Therefore, one can anticipate that the movement of microrollers on endothelial cells will be safe. To test whether the motion of the microrollers is harmful to the endothelial cells, we introduced and then actuated the vast number of microrollers on HUVECs for 5 min at 180 Hz (Figure S11A,B, Supporting Information). After 72 h, the live/dead analysis revealed that almost all of the HUVECs were alive (Figure S11C, Supporting Information) as in the control group, even though many microrollers were still on top of HUVECs. Even though HUVECs were alive, their metabolic activity dropped to 90% compared to the control group (Figure S11D, Supporting Information). This is probably due to the presence of a vast number of microrollers on HUVECs, preventing them from proliferating. The physical and molecular mechanisms behind the 10% drop in metabolic activity need a careful investigation, which is beyond the scope of this study.

The results presented here demonstrated that the FePt coating has almost no adverse effect on macrophages and HUVECs and suggest that the FePt is a promising ferromagnetic material for use in the body. For example, the FePt-coated group showed similar viability levels with the silica (uncoated) group, where silica was extensively investigated in the literature and proved to be a biocompatible material.[23] On the other hand, "biocompatibility" is an application-specific property and does not depend on a single factor (e.g., robot material). It also depends on other factors, such as specific robot size, shape, interacted cell types, and specific target applications.[28] Nevertheless, we have shown that FePt coating enhanced the overall biocompatibility of our microrollers for the given in vitro tests.

2.3. Medical Imaging of FePt-Coated Microrollers

Localization of the microrobots in in vivo conditions is an essential step towards clinical applications of the mobile microrobots.[10,11,29,30] Several imaging modalities have been proposed for tracking microrobots;[10,26] while each imaging modality has advantages in terms of image resolution, penetration depth, and safety, there is a common negative correlation between spatial and temporal resolution for microrobot tracking.[10] For a specific imaging modality, the required spatial resolution for microrobot tracking depends on the imaging modality-dependent contrast agent and its concentration in the microrobot system. Thus, determining the minimum number of visible microrobots in vivo is critical while designing a complete medical scenario. To benefit from the distinct advantages of multiple imaging platforms, we should incorporate multifunctional materials, visible at cross imaging platforms, into microrobots. In addition to the actuation functionality and biocompatibility of the FePt coating, here, we also explored the cross-platform imaging potential of the FePt-coated microrollers using MRI and PA imaging without additional contrast agents.

MRI is a well-established imaging modality used for various clinical practice purposes for a long time.[31] It works based on nuclear spin excitation with a radio-frequency field combined with magnetic field-based spin phase manipulation.[31] MRI can obtain high-resolution 3D anatomical images of soft tissues; therefore, it is a spotlighted imaging modality in microrobotics research.[10] PA is an emerging technique for imaging microrobots, which relies on detecting the emitted ultrasound waves upon the absorption of pulsed laser light from the body tissues.[32] The contrast in PA depends on the optical properties of tissues or microrobots and the applied wavelength of the light.[10] It shows a high promise in the medical microrobotics field since it offers micrometer-resolution, relatively deep tissue, real-time, and wavelength-specific imaging.[33] PA has also been widely used in vascular imaging in preclinical settings,[34] which makes it particularly interesting for our target application.

As mentioned before, the contrast in PA relies on the optical properties of the matter; therefore, we performed UV/Vis/NIR spectrophotometer analysis with uncoated and FePt-coated particles. We have observed that the FePt-coated microrollers gave distinctly higher absorbance than the uncoated ones (Figure S12, Supporting Information), showing the potential of the FePt in PA-based microrobot tracking. Next, we tested the contrast of the uncoated and FePt-coated particles in the PA imaging system. For this, we dispersed and immobilized the particles in an agarose gel with different particle concentrations (0.6, 2.5, 5.0,

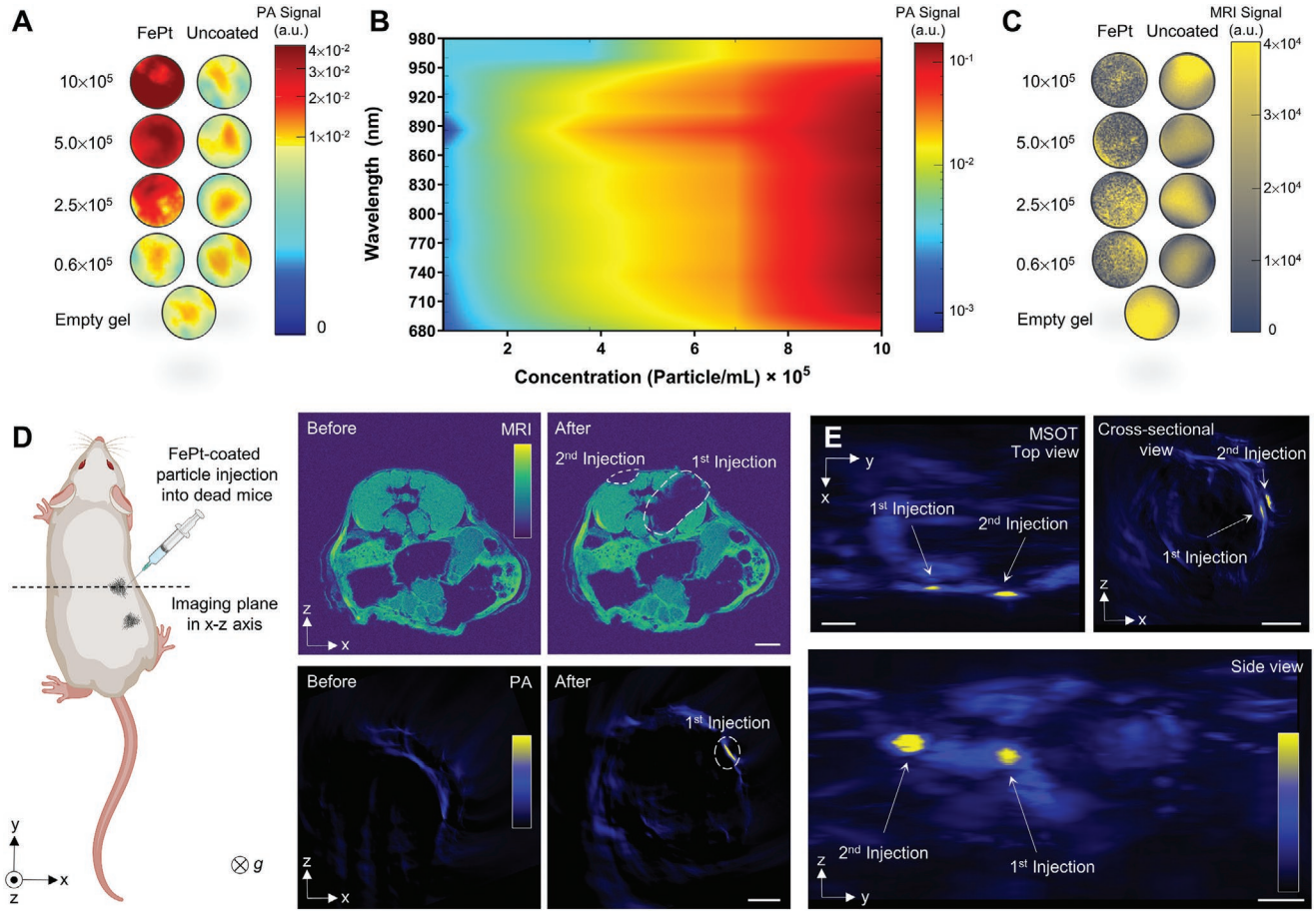

Figure 4. Ex vivo medical imaging of the (60 nm-thick) FePt-coated microrollers using two methods: photoacoustic (PA) imaging and magnetic resonance imaging (MRI). A) Microrollers with different concentrations were embedded into an agarose gel in a 96-well plate, and PA image signals were quantified. The numbers on the left represent the number of microrollers/mL concentrations. The FePt-coated microrollers gave distinct PA image signal (at 860 nm) with increasing concentration, while the signal of the uncoated silica particles was similar to the empty gel. B) The PA image signal of the FePt-coated microrollers was mapped with respect to concentration and wavelength. The PA signal increased with increasing concentration at all wavelengths, where the increase was less prominent at higher wavelengths (i.e., 980 nm). C) T2*-weighted MR imaging of the same particle groups. The magnetic FePt microrollers distorted the MRI signal as expected. D) Ex vivo imaging of the FePt microrollers. 2×10^5 FePt-coated microrollers were injected into the right-leg back of a dead mouse at two different points. The cross-sectional images in MRI and PA images have shown the contrast of the microrollers in the soft tissue. In MRI, the signal was distorted, and particles were visible after injection as a big dark spot. The same spot was much smaller and precisely located in PA images. Scale bar: 2 mm. E) PA projection images of the whole dead mice at 900 nm wavelength. Both injections were visible, where the first injection was deeper than the second one. Accordingly, the first injection gave less signal than the second injection. Scale bar: 5 mm.

and 10×10^5 particles/mL). The FePt-coated microrollers gave increasing localized PA signals with increasing concentration. In contrast, the signal of the uncoated particles was not different from the empty gel at any concentration at an excitation wavelength of 860 nm (**Figure 4**A). Then, we measured the PA signal of the FePt-microrollers at different wavelengths, where we observed a linearly increasing signal with increasing concentration for all wavelengths, while the signal increases at higher wavelengths (i.e., at 980 nm) were less pronounced (Figure 4B).

We performed a similar analysis using a 7-Tesla small-animal preclinical MRI system using the same sample set. We expected the FePt-coated microrollers to give a negative contrast in the T_2*-weighted image due to their high saturation magnetization and consequently to dephase the signal, leading to hypointense signal regions on T_2*-weighted images. We observed that the FePt-coated microrollers increased negative MRI contrast with increasing concentration, whereas the uncoated silica particles did not give significant negative contrast for the same concentrations (Figure 4C). Additionally, due to the high sensitivity of the MRI signal generation mechanism to the local non-uniform magnetic fields, the particles at the lowest concentration, 0.6×10^5 particles/mL, were still visible in MRI. At the same time, they were indistinguishable from the background in PA imaging.

To explore the imaging potential of the FePt-coated microrollers inside the biological tissues, we performed ex vivo experiments using fresh dead mice. We performed whole-body MRI and PA imaging scans of the dead mouse before injection and then injected 2×10^5 microrollers to the back muscle of the dead mouse at two different locations. After the injections, we repeated the whole-body scans to analyze the differences (Figure 4D). T_2*-weighted MRI analysis has shown the microrollers created a local negative contrast around after the

injection and were easy to identify in the axial cross-sectional image (Figure 4D). The microrollers have also given distinct contrast in the PA imaging, and they could be easily identified in a similar cross-sectional slice (Figure 4D,E). Note that the microrollers at the same injection point resulted in different spot sizes of 5.4 × 2.3 mm and 0.11 × 1.17 mm in MRI and PA images, respectively, since ferromagnetic magnetic materials create negative contrast regions multiple ten times than their sizes in MRI.[31] Both microroller injections were visible in the projection PA images, where the deeper injection (1st injection) gave a weaker signal. The results have demonstrated that 2×10^5 microrollers were both visible in MRI and PA. Therefore, we dramatically, 20-fold, decreased the microroller number and tested the visibility of the microrollers using a different fresh dead mouse (Figure S13, Supporting Information). 1×10^4 microrollers again could be detected in MRI as a smaller region; however, the signal of the microrollers could not be differentiated from the animal tissue signals in PA imaging (Figure S13, Supporting Information).

Even though MRI was more sensitive to our magnetic microrollers according to the presented results, it must be noted that integrating an actuation system for the microrollers has serious practical problems, due to the very high static magnetic field inside the MRI bore. The MRI's magnetic field gradients can be used for pulling-based magnetic actuation of the particles we used in this study,[31] however, the field gradients cannot induce rolling but only pulling-based sliding of the particles. Another important consideration is that obtaining a high-resolution MR image requires a relatively long imaging duration that is not feasible for imaging-guided navigation in high fluidic flow environments. Nevertheless, MRI seems to be an optimal imaging modality to localize the microrollers after completing the medical task. On the other hand, PA imaging offers wavelength-specific and high-speed imaging, which is crucial for image-guided navigation. Moreover, integrating the actuation system into a PA system is more straightforward. Overall, the initial imaging experiments of FePt-coated microrollers have shown the great potential of our microrobotic system for future in vivo applications. Furthermore, the contrast-to-noise ratio in the PA can be further enhanced by integrating additional contrast agents, such as indocyanine green (ICG), which will be explored in future studies.

2.4. Photoacoustic Imaging-Guided Propulsion of FePt-Coated Microrollers in Physiological Flows

The microrobots administered through the intravenous (IV) route to the circulatory system must locomote upstream, especially at high flow velocities, to reach the post-capillary venules[35] to efficiently deliver the cargo.[3,30] In an IV injection scenario of passive microparticles, the particles go to the heart and then pass through the pulmonary circuit so that microparticles could be trapped in the lung and cause severe medical problems.[36] Therefore, one should be able to control the microrobots in the circulatory system in a precise manner to prevent severe problems. The vessel walls seem to be the ideal location for the microrobot locomotion, apparently observed in leukocyte migration[37] due to dramatically decreased flow velocities at the walls.

To demonstrate the potential of the FePt-coated microrollers for navigation in the circulatory system, we performed PA imaging-guided upstream locomotion experiments against 4.5 cm s^{-1} continuous phosphate-buffered saline (PBS) flow, mimicking the flows found in veins.[38] We chose to mimic the venous flow since its speed is significantly higher than the velocity of the microroller. Therefore, upstream locomotion ability at such high velocities demonstrates the potential of microrollers in other vessel types having lower average speeds, such as post capillary venules. The magnetically actuated microrollers were injected into a 3 mm diameter tubing at which the PA imaging transducer was fixed on top of it (**Figure 5**A, Figure S14, Supporting Information). First, we performed experiments at static conditions and actuated 3×10^4 microrollers at 180 Hz, 10 mT. Upon actuation, the microrollers started to locomote and left the field of view after 5 s (Figure 5B, Supplementary Video S2). Before actuation, the signal of the microrollers appeared as a small spot. Then the signal was scattered upon actuation due to disaggregation of the microrollers. The signal eventually disappeared since the microrollers left the field of view (Figure 5B, Supporting Information Video S2). In the flow experiments, the same number of microrollers was injected into the tubing and again actuated at 180 Hz, 10 mT. The microrollers again were able to locomote against the fluid flow (4.5 cm s^{-1}), and most of the microrollers were able to leave the field of view in 6 s (Figure 5C, Supporting Information Video S2). The microrollers gave a scattered signal before actuation (Supporting Information Video S2), unlike the static case. In other words, they were relatively disaggregated due to flow conditions. This is probably because microroller swarms behave differently in different media, and the swarming behavior of microrollers under different conditions requires detailed investigation, which is beyond the scope of this study.

The tubing was located diagonally on the x–y plane in the experiments (Figure 5B,C); therefore, the other imaging planes do not fully show the tubing cross-section from radial and side view. From the same experiments, we also presented the translational motion of the microrollers from the side view of the tubing (Figure S15A–C, Supporting Information). Additionally, the microrollers must also locomote in 3D due to the nature of the vascular system. As explained and demonstrated in our previous report,[3] propulsion force generated by microrollers in less than 8 μm dominates the gravitational force term. This enables the movement of the microrollers on the inclined or curved surfaces as well. Therefore, climbing or moving on a curved surface is not an issue for rolling microrobots as long as they can break the symmetry by the presence of a near wall. We also presented the locomotion of the microrollers on inclined surfaces with PA imaging (Figure S15D, Supporting Information), where the microrollers successfully climbed the wall.

We performed computational fluid dynamics (CFD) analyses to elucidate how microrollers could locomote in such high flow velocities, where the speed of a single microroller is around 400–500 μm s^{-1} but the average flow velocity in the tubing is 4.5 cm s^{-1}. The simulations were conducted based on the dimensions and the flow velocities used in the experimental setup. The results showed the parabolic flow profile in the circular-cross section tubing, as in blood flowing in veins,[37–39] where the flow velocities were multiple times lower than on the

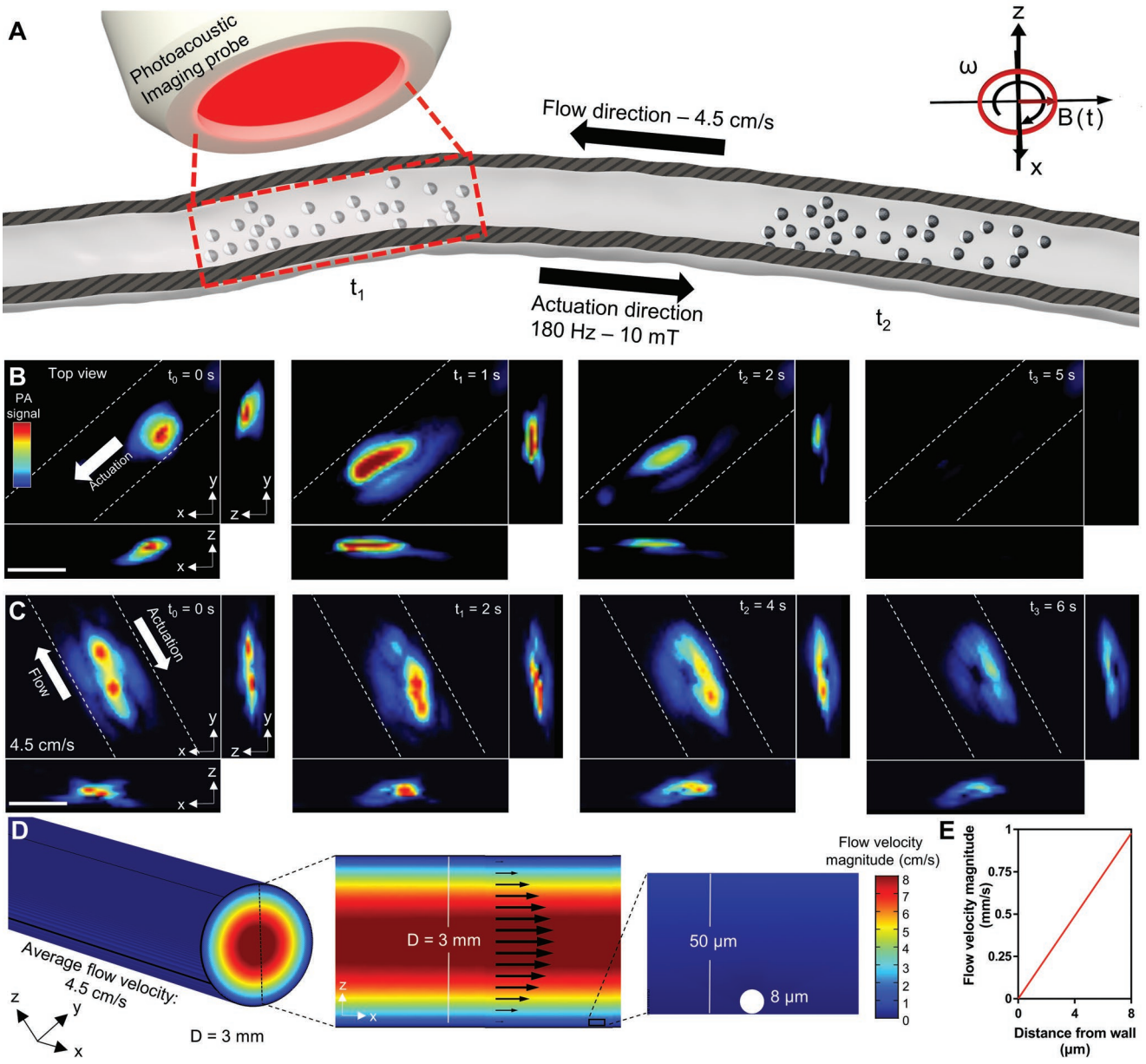

Figure 5. Photoacoustic (PA) imaging-guided upstream locomotion of the FePt-coated (60 nm-thick) microrollers against 4.5 cm s^{-1} PBS flow. A) Experimental procedure schematics. The position of the PA transducer was kept the same, while the microrollers left the field-of-view upon magnetic actuation to the predefined actuation direction. B) Time-lapse PA images of 3×10^4 microrollers actuated in the tubing at static conditions. Upon actuation at 180 Hz, the microrollers were locomoted in the tubing and left the field of view after 5 s. The dashed lines represent the position of the tubing. The gravity acts in the negative *z*-direction. Scale bar: 3 mm. C) Time-lapse PA images of 3×10^4 microrollers actuated at 4.5 cm s^{-1} average flow velocity in the tubing. The microrollers were able to locomote against the flow, and most of the microrollers were able to leave the field of view after 6 s. The gravity acts in the negative *z*-direction. Scale bar: 3 mm. D) Computational fluid dynamics (CFD) analysis of the flow experiments. 4.5 cm s^{-1} fluid flow was simulated in 3 mm tubing as in the experiments, where the flow velocity magnitude at the tubing wall was dramatically smaller than the center. E) The flow velocity magnitude near the tubing wall is comparable to the microroller speeds at the 8 µm distance.

tubing walls (Figure 5D). Specifically, 8 µm above the tubing wall, the flow velocities were comparable to the microroller speeds at 180 Hz (Figure 5E), which explains the upstream locomotion ability of the microrollers. Of note, the CFD model and experiments presented here are very simplistic compared to the hemodynamics in blood vessels. The realistic modeling of blood requires advanced features such as deformability of red blood cells and non-Newtonian elements,[40] which is beyond the scope of this study. Still, it is known that blood flow in veins acts as a Poisuelle flow,[41] which we also have in our simulations. Overall, the locomotion ability of the microrollers demonstrated a high potential for navigation in the endovascular system for future in vivo targeted cargo (e.g., drug, gene, and imaging agent) delivery applications.

3. Conclusions

We integrated FePt ($L1_0$) magnetic alloy into our microroller system, and the new coating has shown promise from different aspects, such as magnetic actuation performance, biocompatibility, and medical imaging. The presented magnetic material outperformed the previously used magnetic material (Ni) and resulted in at least two times better performance due to its higher remanence. This is especially important for endovascular applications of magnetic microrobots, where stronger magnetic materials are needed to overcome harsh fluidic flows. We have also observed that increasing the FePt film thickness did not lead to a proportional increase in the performance; thus, the new nanofabrication schemes must be explored to obtain the maximum efficiency from the magnetic thin film.[42] For example, 60 nm-thick nanofilm resulted in the best remanence and coercivity. Thus, thicker nanofilms with an inert layer between multiple 60 nm-thick nanofilms might increase the propulsion performance. However, we also observed higher remanence also caused aggregation of high-density microrollers, which can be eliminated by integrating a thick inert layer on top of the microrollers to disaggregate them upon actuation. Another important consideration is that the FePt nanofilm can only be integrated into mostly ceramic-based materials due to the high processing temperature above 680 °C. Integration of the FePt film is possible on 3D complex robot bodies thanks to the advancements in two-photon lithography.[43]

Biocompatibility of the microrobot materials is very critical, which was often overlooked in microrobotic studies. The previously shown biocompatible magnetic materials used in microrobotic studies suffered from low remanence, therefore, low performance.[44] The FePt alloy meets both requirements, which makes FePt-based systems promising for future medical applications. The other important consideration, arguably the most, is medical imaging of microrobots in vivo. We explored the multimodal medical imaging potential of the FePt-coated microrollers using PA imaging and MRI, without incorporating any contrast agents. We detected a relatively low number of microrollers inside ex vivo soft tissues in dead mice towards future in vivo medical applications.

The microrollers were also able to locomote against high-speed fluid flows, specifically found in veins, along with real-time PA imaging. The results presented here demonstrate the potential of microrobotic systems to be used in the endovascular targeted delivery applications for the treatment of certain diseases (e.g., cancer). The future work will focus on performing a medical scenario (e.g., drug/gene delivery,[45] treatment of cerebral aneurysm[15]) using microroller swarms in a realistic setting (e.g., in vivo). Reaching such challenging goals is only possible using advanced materials, such as FePt ($L1_0$), due to its unique advantages. We envision the FePt ($L1_0$) alloy as one of the key materials for magnetic microrobotic systems to be used in future clinical applications.

4. Experimental Section

Fabrication of Magnetic Microrollers: Silica particle monolayers (7.82 µm diameter, microParticles GmbH) were prepared using the drop-casting method on an oxygen plasma-treated Si wafer. Plasma treating of the wafer was a necessary step to render a hydrophilic surface, to make a monolayer formation possible. After the monolayers were formed, samples were fully dried for a few hours at room temperature under ambient conditions to prevent any possible damage in the molecular beam epitaxy (MBE) chamber and preserve the ultra-high vacuum (UHV) conditions. All the microrollers tested and discussed in this work were prepared in the MBE system under UHV conditions (≈2 to 5×10^{-9} mbar). Once the samples were placed inside the main chamber, the surface was blocked using the main shutter of the system. Fe was evaporated from an effusion cell, Pt from an electron beam evaporator. Both were manually controlled to achieve desired deposition rates. The deposition rate of the process was observed for each material separately using a quartz balance. The deposition rate for Fe and Pt was 0.3 Å s^{-1}, measured by a quartz balance. Therefore, the atomic composition range of 50% for each material was achieved. Precise control of the percentage of the deposited material was crucial to ensure the $L1_0$ phase formation. The region to obtain the $L1_0$ phase can be marked at approximately 35 to 55 atomic percent of Pt over the binary phase diagram of Fe–Pt.[15] During the deposition, the substrate holder was constantly rotating to have a homogenous layer of a thin film. 60, 120, and 480 nm of FePt films co-deposited at room temperature. The deposition process was followed by the heat treatment of the samples at 680 °C, in the same chamber without breaking the UHV conditions. After 1 h of annealing, the samples were cooled down and were taken out for further characterization. For Ni-coated samples, 20 nm of Au layer was added as a passivation layer to prevent non-specific attachment of Ni-coated particles. XRD measurements were done with Bruker AXS D8Discover-DaVinci spectrometer using sealed tube Cu-anode, 1D parallel beam Goebel mirror, and LynxEye 1D-detector manufactured by Bruker. XPS measurements were conducted with Thermo Fisher Theta Probe System for Angle-Resolved X-Ray Photoelectron Spectroscopy (ARXPS). Magnetic characterizations were performed with VSM (MicroSense, Lowell, MA), and microrollers were programmed in different directions by applying 1.8 Tesla uniform magnetic field.

Magnetic Field Control: The magnetic microrollers were actuated using a custom-built five coiled electromagnetic coil (4 xy-coils and 1 z-coil) system. 2.5 mT out-of-plane rotating magnetic field was applied to investigate the step-out frequencies of different microroller groups. The mean speeds of microrollers were analyzed using in-house MATLAB code that performs object detection and tracking. Imaging-guided upstream locomotion experiments were performed using a 3 mm diameter plastic tubing connected to a syringe pump (KD Scientific Inc., Holliston, MA). The known number of microrollers (60 nm-thick FePt-coated) were injected into the tubing using a syringe. A 10 mT out-of-plane rotating magnetic field was applied to actuate the microrollers in static and flow conditions.

Cell Culture, Biocompatibility Tests, and Cell Staining Experiments: Mouse macrophage-like cells, J774A.1, were obtained from the American Type Culture Collection (ATCC, Rockville, MD, USA). The cells were cultured in Dulbecco's modified Eagle's medium supplemented with 10% (v/v) fetal bovine serum, penicillin (50 UI mL^{-1}), and streptomycin (50 µg mL^{-1}) in a humidified, 37 °C, 5% CO_2 environment using 75 cm^2 polystyrene cell culture flasks. For biocompatibility tests, J774A.1 cells were seeded at a concentration of 1×10^4 cells/100 µL into µ-slide eight-well chambered Ibidi Polymer (ibiTreat) coverslips. After allowing cells to attach overnight, the cells were treated with silica (uncoated), Ni-(60–20 nm Au), and FePt (60 nm)-coated particle groups with 1:10 particle to initial number of cell ratio. After 48, 72, and 96 h of particle addition, esterase activity (Calcein-AM) of the cells were investigated using LIVE/DEAD Viability/Cytotoxicity Kit (Invitrogen, Thermo Fisher Scientific, Waltham, MA). The staining solution was incubated at room temperature for 20 min before being observed using a fluorescence microscope (Nikon Eclipse Ti-E, Tokyo, Japan). The live cells were imaged and analyzed with Fiji software. Each specific group had a triplicate of samples (e.g., 48 h–FePt group had at least 3 Ibidi well plates, 27 well plates in total for all groups), and esterase activity of the particle-macrophages complexes was captured from Ibidi well plates. At

least 300 particle-macrophage complexes were captured for each specific well for viability assessment. The viability from each well was calculated from the equation below:

$$\%\ \text{Cell viability} = \frac{\text{Number of Calcein} - \text{AM active particle} - \text{macrophage compelexes}}{\text{Number of total particle} - \text{macrophage complexes}} \times 100 \quad (1)$$

The mean and standard deviations were calculated from the triplicates from each specific group.

Human umbilical vein endothelial cells (HUVECs) were obtained from the American Type Culture Collection (ATCC, Rockville, MD, USA). HUVECs were grown in endothelial cell growth basal medium 2 (CC-3156, Lonza) supplemented with endothelial cell growth media 2 SingleQuots (CC-4176, Lonza) in a 5% CO_2, 95% air humidified atmosphere using 75 cm^2 polystyrene cell culture flasks. For the dose-dependent viability tests, the macrophages and HUVECs were seeded into a 96-well plate at the concentration of 10^4 cells/well. The FePt-coated microrollers were added in 1:10 and 1:2 microroller to initial cell number ratio 24 h after seeding. After 72 h of addition of the microrollers, the viability of the cells was analyzed by The CellTiter-Glo Luminescent Cell Viability Assay, using 1:1 media to reagent ratio. The luminescence was measured in opaque 96-well plates with a plate reader (BioTek Gen5 Synergy 2, Bad Friedrichshall). The relative % cell viability was calculated against the control/untreated group. For the dynamic viability tests, the FePt-coated microrollers were added after HUVECs reached the confluence. After, the FePt-coated microrollers were added and actuated on top of the HUVECs for 5 min at 180 Hz. Then the viability of cells was evaluated after 72 h using The CellTiter-Glo Luminescent Cell Viability Assay, using the same protocol above.

For the confocal optical microscope images, the cells and the particles were stained to different fluorescent markers. The silica side of the 60 nm-thick FePt-coated microrollers was modified with Cy5 streptavidin. To do this, 5% v/v (3-Aminopropyl)triethoxysilane solution in ethanol were vortexed with 1×10^6 microrollers overnight and then incubated at 65 °C for 3 h to introduce amino groups on the silica surface. The microrollers were extensively washed with ethanol and then dimethyl sulfoxide (DMSO). Amino groups on the silica surface were reacted with NHS-Biotin (EZ-Link NHS-Biotin, Thermo Fisher Scientific, Waltham, MA). NHS-Biotin, 5 mg mL^{-1} in DMSO, were vortexed with the microrollers for 3 h. After, the microrollers were washed with DMSO and PBS 1×. As the last step, the microrollers were treated with fluorescently labeled streptavidin (Alexa Fluor 647 conjugate, 50 µg mL^{-1} in PBS 1×, Thermo Fisher Scientific, Waltham, MA) for 1 h and then dispersed in PBS 1×. The actin filaments and nuclei of the cells were stained with ActinGreen 488 (Invitrogen, Thermo Scientific, Waltham, MA) and Hoechst 33 342 (Thermo Scientific, Waltham, MA). For the staining, the medium was discarded, cells were rinsed with PBS 1 × and fixed with 4% (w/v) paraformaldehyde (10 min). After rinsing paraformaldehyde solution with PBS 1×, the cells were then permeabilized using 0.1% Triton X-100 in PBS 1×. Then, the cells were incubated for 30 min with ActinGreen 488 diluted in PBS 1×, rinsed again, and incubated with 1 µg mL^{-1} Hoechst 33342 dye diluted in PBS 1×, for another 10 min. The cells were finally rinsed with PBS 1×, and the Ibidi chambers were immediately analyzed by confocal microscopy (Leica SP8 confocal microscope, Wetzlar, Germany).

Light Absorption Spectroscopy and Imaging Experiments with PA Imaging and MRI: The initial optical properties of uncoated (silica) and FePt-coated (60 nm-thick) particles were characterized with a UV/Vis/NIR spectrophotometer (PerkinElmer Lambda 1050) with 1.5×10^6 particle/mL concentration, using a quartz crystal cuvette. The contrast of the uncoated (silica) and FePt-coated particles were tested with different concentrations (0.6, 2.5, 5.0, and 10×10^5 particles/mL), where the particles were dispersed and immobilized in 1% w/v agarose in 96-well plates. A handheld, 3D photoacoustic transducer (256-element transducer, iThera Medical) was used for PA characterization, where the PA signal of the different groups was measured at different wavelengths. The sample set was also used for MRI characterization. MRI experiments were performed on a 7 Tesla Bruker BioSpec (Ettlingen, Germany) using an actively shielded gradient system (BGA20SHP) and 40 mm quadrature birdcage coil. Multi-echo gradient-echo imaging sequence (TR = 3000 ms, 10 echoes, TE = 4–32.3 ms, 1012 μm^2 in-plane resolution, 1 mm slice thickness, NEX = 2) was used to image different concentrations of uncoated and FePt-coated microrollers. Gradient echo imaging sequence (TR/TE 1200/8 ms, 652 μm^2 in-plane resolution, slice thickness of 0.4 mm NEX = 4) was used to image mice (N = 4) before and after injection of 1×10^4 and 2×10^5 FePt microrollers.

For ex vivo imaging experiments, we performed a whole-body scan of the dead mice before and after microroller injection (1×10^4 and 2×10^5 microrollers). FePt microrollers were injected into the back muscle0073 of the dead mice using a syringe with a 30 G needle. The whole-body scan was performed in a Multispectral optoacoustic tomography device (MSOT 512-element transducer, iThera Medical) system with a scanning step of 0.3 mm at different wavelengths. The body scan was also performed in MRI using the same mice with T_2*-weighted Flash sequence (TE/TR = 8/1200 ms) having a slicing thickness of 0.4 µm and field of view 26×26 mm^2.

COMSOL Simulations: COMSOL Multiphysics 5.5 Simulation Software (COMSOL, Inc.) was used to estimate flow velocity magnitudes. Simulations were performed in 3D, by solving Navier–Stokes equations with a 3 mm inner diameter tubing with a 4.5 cm s^{-1} DI water flow. Boundaries of the tubing were defined as no-slip boundaries.

Statistical Analysis: All the quantitative values are presented as means ± standard deviation. All the quantitative experiments were performed with at least three replicates for each group. Student's t-test was used for statistical analysis, and a p-value of less than 0.05 was considered statistically significant.

Supporting Information

Supporting Information is available from the Wiley Online Library or from the author.

Acknowledgements

U.B. and E.S. contributed equally to this work. This work is funded by the Max Planck Society. The authors thank Max Planck Institute for Biological Cybernetics Tübingen (reg: DE 08 416 1083 21) for providing animal side products to MPI Intelligent Systems in Stuttgart (reg: DE 08 111 1008 21) to perform the ex vivo dead mice experiments.

Open access funding enabled and organized by Projekt DEAL.

Conflict of Interest

The authors declare no conflict of interest.

Data Availability Statement

The data that supports the findings of this study are available in the supplementary material of this article.

Keywords

Biocompatible materials, circulatory system, FePt, magnetic microrobots, medical imaging, medical microrobots

Received: October 10, 2021
Published online:

[1] M. Sitti, *MobileMicrorobotics*, MIT Press, Cambridge, MA **2017**.
[2] B. J. Nelson, I. K. Kaliakatsos, J. J. Abbott, *Annu. Rev. Biomed. Eng.* **2010**, *12*, 55.
[3] Y. Alapan, U. Bozuyuk, P. Erkoc, A. C. Karacakol, M. Sitti, *Sci. Rob.* **2020**, *5*, eaba5726.
[4] U. Bozuyuk, Y. Alapan, A. Aghakhani, M. Yunusa, M. Sitti, *Proc. Natl. Acad. Sci. USA* **2021**, *118*, e2022090118.
[5] H. Xu, M. Medina-Sánchez, M. F. Maitz, C. Werner, O. G. Schmidt, *ACS Nano* **2020**, *14*, 2982.
[6] L. Leyssens, B. Vinck, C. Van Der Straeten, F. Wuyts, L. Maes, *Toxicology* **2017**, *387*, 43.
[7] G. Genchi, A. Carocci, G. Lauria, M. S. Sinicropi, A. Catalano, *Int.l J. Environ. Res. Public Health* **2020**, *17*, 679.
[8] K. Son, G. Ryu, H.-H. Jeong, L. Fink, M. Merz, P. Nagel, S. Schuppler, G. Richter, E. Goering, G. Schütz, *Small* **2019**, *15*, 1902353.
[9] V. M. Kadiri, C. Bussi, A. W. Holle, K. Son, H. Kwon, G. Schütz, M. G. Gutierrez, P. Fischer, *Adv. Mater.* **2020**, *32*, 2001114.
[10] A. Aziz, S. Pane, V. Iacovacci, N. Koukourakis, J. Czarske, A. Menciassi, M. Medina-Sánchez, O. G. Schmidt, *ACS Nano* **2020**, *14*, 10865.
[11] M. Medina-Sánchez, O. G. Schmidt, *Nat. News* **2017**, *545*, 406.
[12] S. Maenosono, T. Suzuki, S. Saita, *J. Magn. Magn. Mater.* **2008**, *320*, L79.
[13] Y. Liu, P.-C. Wu, S. Guo, P.-T. Chou, C. Deng, S.-W. Chou, Z. Yuan, T.-M. Liu, *Photoacoustics* **2020**, *19*, 100179.
[14] S.-W. Chou, C.-L. Liu, T.-M. Liu, Y.-F. Shen, L.-C. Kuo, C.-H. Wu, T.-Y. Hsieh, P.-C. Wu, M.-R. Tsai, C.-C. Yang, K.-Y. Chang, M.-H. Lu, P.-C. Li, S.-P. Chen, Y.-H. Wang, C.-W. Lu, Y.-A. Chen, C.-C. Huang, C.-R. C. Wang, J.-K. Hsiao, M.-L. Li, *Biomaterials* **2016**, *85*, 54.
[15] A. C. Bakenecker, A. von Gladiss, H. Schwenke, A. Behrends, T. Friedrich, K. Lüdtke-Buzug, A. Neumann, J. Barkhausen, F. Wegner, T. M. Buzug, *Sci. Rep.* **2021**, *11*, 14082.
[16] T. O. Tasci, D. Disharoon, R. M. Schoeman, K. Rana, P. S. Herson, D. W. M. Marr, K. B. Neeves, *Small* **2017**, *13*, 1700954.
[17] O. Gutfleisch, J. Lyubina, K.-H. Müller, L. Schultz, *Adv. Eng. Mater.* **2005**, *7*, 208.
[18] S. Zhang, D. Zhao, *Advances in Magnetic Materials: Processing, Properties, and Performance*, CRC press, Boca Raton, FL **2017**.
[19] A. Breitling, *Magnetische L10-FePt Nanostrukturen für höchste Datenspeicherdichten*, Cuvillier Verlag, Göttingen **2009**.
[20] K. E. Peyer, L. Zhang, B. J. Nelson, *Nanoscale* **2013**, *5*, 1259.
[21] S. Wang, X. Liu, Y. Wang, D. Xu, C. Liang, J. Guo, X. Ma, *Nanoscale* **2019**, *11*, 14099.
[22] E. Denkhaus, K. Salnikow, *Crit. Rev. Oncol. Hematol.* **2002**, *42*, 35.
[23] H. Jaganathan, B. Godin, *Adv. Drug Delivery Rev.* **2012**, *64*, 1800.
[24] a) B. Godin, J. Gu, R. E. Serda, R. Bhavane, E. Tasciotti, C. Chiappini, X. Liu, T. Tanaka, P. Decuzzi, M. Ferrari, *J. Biomed. Mater. Res., Part A* **2010**, *94A*, 1236; b) E. Tasciotti, B. Godin, J. O. Martinez, C. Chiappini, R. Bhavane, X. Liu, M. Ferrari, *Mol. Imaging* **2011**, *10*, 56; c) R. E. Serda, S. Ferrati, B. Godin, E. Tasciotti, X. Liu, M. Ferrari, *Nanoscale* **2009**, *1*, 250; d) R. E. Serda, A. Mack, M. Pulikkathara, A. M. Zaske, C. Chiappini, J. R. Fakhoury, D. Webb, B. Godin, J. L. Conyers, X. W. Liu, J. A. Bankson, M. Ferrari, *Small* **2010**, *6*, 1329.
[25] a) T. Yu, A. Malugin, H. Ghandehari, *ACS Nano* **2011**, *5*, 5717; b) M. V. Baranov, M. Kumar, S. Sacanna, S. Thutupalli, G. van den Bogaart, *Front. Immunol.* **2021**, *11*, 3854.
[26] D. Hirayama, T. Iida, H. Nakase, *Int. J. Mol. Sci.* **2018**, *19*, 92.
[27] D. Gonzalez-Rodriguez, L. Guillou, F. Cornat, J. Lafaurie-Janvore, A. Babataheri, E. de Langre, A. I. Barakat, J. Husson, *Biophys. J.* **2016**, *111*, 2711.
[28] D. F. Williams, *Biomaterials* **2014**, *35*, 10009.
[29] a) A. Aziz, M. Medina-Sánchez, N. Koukourakis, J. Wang, R. Kuschmierz, H. Radner, J. W. Czarske, O. G. Schmidt, *Adv. Funct. Mater.* **2019**, *29*, 1905272; b) A. C. Hortelao, C. Simó, M. Guix, S. Guallar-Garrido, E. Julián, D. Vilela, L. Rejc, P. Ramos-Cabrer, U. Cossío, V. Gómez-Vallejo, T. Patiño, J. Llop, S. Sánchez, *Sci. Rob.* **2021**, *6*, eabd2823.
[30] Q. Wang, K. F. Chan, K. Schweizer, X. Du, D. Jin, S. C. H. Yu, B. J. Nelson, L. Zhang, *Sci. Adv.* **2021**, *7*, eabe5914.
[31] O. Erin, M. Boyvat, M. E. Tiryaki, M. Phelan, M. Sitti, *Adv. Intell. Syst. 20202*, 1900110.
[32] C. Lutzweiler, D. Razansky, *Sensors* **2013**, *13*, 7345.
[33] a) A. Aziz, J. Holthof, S. Meyer, O. G. Schmidt, M. Medina-Sánchez, *bioRxiv* **2020**, 2020.06.15.148791; b) Z. Wu, L. Li, Y. Yang, P. Hu, Y. Li, S.-Y. Yang, L. V. Wang, W. Gao, *Sci. Rob.* **2019**, *4*, eaax0613; c) L. Xie, X. Pang, X. Yan, Q. Dai, H. Lin, J. Ye, Y. Cheng, Q. Zhao, X. Ma, X. Zhang, G. Liu, X. Chen, *ACS Nano* **2020**, *14*, 2880; d) Y. Yan, W. Jing, M. Mehrmohammadi, *Sensors* **2020**, *20*, 2816.
[34] a) A. B. E. Attia, G. Balasundaram, M. Moothanchery, U. S. Dinish, R. Bi, V. Ntziachristos, M. Olivo, *Photoacoustics* **2019**, *16*, 100144; b) S. Gottschalk, O. Degtyaruk, B. Mc Larney, J. Rebling, M. A. Hutter, X. L. Deán-Ben, S. Shoham, D. Razansky, *Nat. Biomed. Eng.* **2019**, *3*, 392; c) E. Z. Zhang, J. G. Laufer, R. B. Pedley, P. C. Beard, *Phys. Med. Biol.* **2009**, *54*, 1035.
[35] K. Kucharz, K. Kristensen, K. B. Johnsen, M. A. Lund, M. Lønstrup, T. Moos, T. L. Andresen, M. J. Lauritzen, *Nat. Commun.* **2021**, *12*, 4121.
[36] C. Voukalis, E. Shantsila, G. Y. H. Lip, *Ann. Med.* **2019**, *51*, 193.
[37] O. K. Baskurt, M. R. Hardeman, M. W. Rampling, *Handbook of Hemorheology and Hemodynamics*, IOS press, Amsterdam, Washington **2007**.
[38] M. Klarhöfer, B. Csapo, C. Balassy, J. C. Szeles, E. Moser, *Magn. Reson. Med.* **2001**, *45*, 716.
[39] J. Garcia-Duitama, B. Chayer, D. Garcia, Y. Goussard, G. Cloutier, *Ultrasound Med. Biol.* **2017**, *43*, 2871.
[40] G. Závodszky, B. van Rooij, V. Azizi, A. Hoekstra, *Front. Physiol.* **2017**, *8*, 563.
[41] J. J. Bishop, A. S. Popel, M. Intaglietta, P. C. Johnson, *Biorheology* **2001**, *38*, 263.
[42] Z. L. Zhao, J. S. Chen, J. Ding, J. B. Yi, B. H. Liu, J. P. Wang, *Appl. Phys. Lett.* **2006**, *88*, 052503.
[43] F. Kotz, A. S. Quick, P. Risch, T. Martin, T. Hoose, M. Thiel, D. Helmer, B. E. Rapp, *Adv. Mater.* **2021**, *33*, 2006341.
[44] a) U. Bozuyuk, O. Yasa, I. C. Yasa, H. Ceylan, S. Kizilel, M. Sitti, *ACS Nano* **2018**, *12*, 9617; b) P. Cabanach, A. Pena-Francesch, D. Sheehan, U. Bozuyuk, O. Yasa, S. Borros, M. Sitti, *Adv. Mater.* **2020**, *32*, 2003013.
[45] M. B. Fish, A. L. Banka, M. Braunreuther, C. A. Fromen, W. J. Kelley, J. Lee, R. Adili, M. Holinstat, O. Eniola-Adefeso, *Sci. Adv.* **2021**, *7*, eabe0143.